Astron. Astrophys. 327, 467–478 (1997)

ASTRONOMY
AND
ASTROPHYSICS

Properties of optically and X-ray selected quasars

G. Lamer[1⋆,⋆⋆], **H. Brunner**[2,⋆], **and R. Staubert**[1]

[1] Institut für Astronomie und Astrophysik, Abt. Astronomie, Universität Tübingen, Waldhäuserstr. 64, D-72076 Tübingen, Germany
[2] Astrophysikalisches Institut Potsdam, An der Sternwarte 16, D-14482 Potsdam, Germany

Received 6 March 1997 / Accepted 4 June 1997

Abstract. We have performed optical spectroscopy on 31 quasars and 8 narrow emission line objects identified from X-ray sources in two ROSAT PSPC fields at high galactic latitudes. The broad band and X-ray spectral properties of the quasars have been investigated and are compared with the properties of optically selected quasars observed with ROSAT in one of the two fields.

We find that optically luminous objects at high redshifts are relatively underluminous in X-rays and discuss attempts to disentangle the relations of $\alpha_{\rm ox}$ with luminosity and redshift. Based on simulations of the quasar samples we show that multivariate regression methods applied to the $\alpha_{\rm ox}$ ($l_{\rm opt}$, z) and $\alpha_{\rm ox}$ ($l_{\rm x}$, z) relations can yield misleading results as $\alpha_{\rm ox}$ and the luminosities are not statistically independent quantities. For our two samples we find that the $\alpha_{\rm ox}$ (l, z) relations of the optically and X-ray selected samples are consistent with each other, not confirming previous claims about a difference.

In both samples the mean X-ray spectra become flatter with increasing redshift. We conclude that the X-ray spectra of the low redshift objects are dominated by a soft excess component which is shifted out of the PSPC sensitivity window for higher redshifts. From the X-ray spectral and broad band properties in our X-ray selected sample we conclude that intrinsic absorption does not play a role in the quasar sample but in some of the narrow line objects.

Our overall results are consistent with the view that both optically and X-ray selected samples are drawn from the same population of objects.

Key words: galaxies: active – quasars: general – galaxies: Seyfert – X-rays: galaxies

Send offprint requests to: G. Lamer

⋆ Visiting Astronomer, German-Spanish Astronomical Center, Calar Alto, operated by the Max-Planck-Institut Heidelberg jointly with the Spanish National Commission for Astronomy

⋆⋆ Visiting Astronomer, European Southern Observatory, La Silla, Chile

1. Introduction

X-ray emission is a common property of all types of quasars and is thought to originate in the innermost regions of the objects. In particular, the soft X-ray "excess" component (e. g. Arnaud et al. 1985) is believed to be associated with the thermal emission from an accretion disk. As a consequence of the soft excess the average quasar spectrum is significantly steeper in the ROSAT PSPC band (0.1-2.4 keV) than previously measured at higher energies (e.g. Brunner et al. 1992). Since the launch of the ROSAT satellite the observational situation in soft X-rays has significantly improved. The high sensitivity of the ROSAT PSPC allows the study of AGN at higher redshifts as compared to the previous *Einstein* observations. Identifications of X-ray sources from pointed ROSAT observations (Boyle et al. 1993, 1995, Puchnarewicz et al. 1996) have resulted in X-ray selected quasar samples having lower flux limits and higher mean redshifts than the *Einstein* Extended Medium Sensitivity Survey (EMSS, Gioia et al. 1990). The ROSAT samples significantly improve our knowledge of the quasar luminosity function and the contribution of AGN to the X-ray background (e.g. Hasinger et al. 1993, Comastri et al. 1995).

We have performed deep pointed ROSAT PSPC observations with a total integration time $t_{\rm int}$ = 80 ksec in a $2.2^\circ \times 2.2^\circ$ field of the optical CFHT quasar survey (Crampton et al. 1989). The ROSAT observations provide homogeneous X-ray data for the 149 CFHT quasars and resulted in the detection of 65 objects (44%). The analysis of the ROSAT data of the optically selected QSOs and modeling of their X-ray properties with an accretion disk model is described by Brunner et al. (1997, Paper I).

This paper reports on optical follow up identifications of additional X-ray sources in the CFHT survey field and in a comparison field of similar galactic latitude and absorbing column density. Sect. 2 describes the data analysis and contains the basic data of the newly identified objects. In Sect. 3 we compare the properties of the X-ray selected and optically selected samples and present simulations of the samples. Finally, Sect. 4 summarizes the results and gives a comparison with investigations of other authors.

Table 1. ROSAT observations

ROR No	α(2000)	δ(2000)	$t_{\rm int}$ [s]	completed
		SGP field:		
CA150033	01 37 38	-24 30 36	6374	21-sep-91
		CFHT field:		
WG701062	13 36 17	27 04 48	9461	14-jul-92
WG701063	13 42 50	27 04 48	10044	22-jul-92
WG701064	13 37 36	26 37 48	8356	13-jul-92
WG701065	13 37 36	27 31 48	8973	11-jul-92
WG701066	13 39 34	26 21 00	9050	14-jul-92
WG701067	13 39 31	27 49 12	8214	15-jul-92
WG701068	13 41 31	26 37 48	8669	17-jul-92
WG701069	13 41 29	27 31 48	9916	14-jul-92
WG701459	13 39 34	27 04 48	7209	09-jul-93

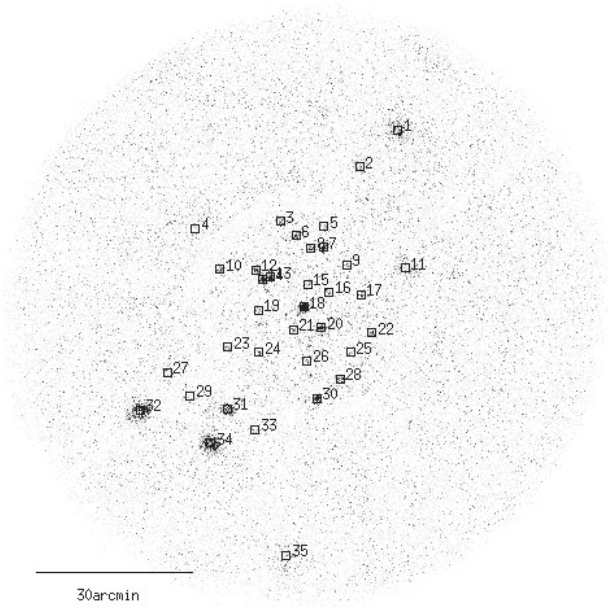

Fig. 1. ROSAT PSPC image of the SGP field with source numbers.

2. Observations and data analysis

2.1. X-ray data

Two fields were observed with the PSPC detector onboard the ROSAT satellite:

- a single pointing on the quasar *PKS 0135-247* near the south galactic pole (SGP-field).
- a mosaic of 9 pointings covering a field of the optical quasar survey performed by Crampton et al. (1989) with the *Canada-France-Hawaiian Telescope* (CFHT-field).

Tab. 1 gives details of these PSPC observations. Both fields have very low galactic hydrogen column densities (SGP: $N_{\rm H}$ =1.27 $\cdot$ 10^{20}cm^{-2}, CFHT: $N_{\rm H}$ =1.05 $\cdot$ 10^{20}cm^{-2}, Stark et al. 1992). Low $N_{\rm H}$ significantly increases the sensitivity for the detection of extragalactic sources as the ROSAT PSPC has its largest effective area below 0.3 keV where interstellar absorption mostly by Helium atoms is strong.

2.1.1. SGP field

Due to deterioration of the X-ray telescopes (XRT) point spread function at higher off-axis angles the point source sensitivity of a ROSAT pointing is not uniform throughout the PSPC field of view. The on-axis sensitivity of the SGP observation expressed as minimum flux density at 1 keV is $f_{\rm lim} \simeq 4$ nJy $\simeq 10^{-14}$erg/(cm^2 s keV).

In the PSPC image of the SGP observation 35 X-ray sources have been detected by the ROSAT *Standard Analysis Software System* (SASS) at significance levels $-\ln P \geq 12$ where P is the likelihood for a spurious detection. See Fig. 1 for the PSPC image with source numbers indicated. Note that the target of the ROSAT observation, PKS 0135-247, was omitted in the statistical investigations of the X-ray sources.

Assuming power law spectra and galactic absorption with $N_{\rm H}$ =1.27 $\cdot$ 10^{20}cm^{-2} spectral energy indices $\alpha_{\rm x}$ of the sources have been derived from the SASS hardness ratios

$$hr = \frac{cr_{\rm hard} - cr_{\rm soft}}{cr_{\rm hard} + cr_{\rm soft}}$$

with the countrates $cr_{\rm hard}$ and $cr_{\rm soft}$ in the hard (0.4-2.4 keV) and the soft (0.1-0.4 keV) bands by using an interpolation table. This table contains pairs of spectral indices and hardness ratios and was created by folding a set of absorbed ($N_{\rm H}$ =1.27 $\cdot$ 10^{20}cm^{-2}) power law spectra with the PSPC detector response. Flux densities at 1 keV were derived from the total countrates (0.1-2.4 keV) using the conversion

$$f_\nu[\mu{\rm Jy}](1\ {\rm keV}) = 1.385 \cdot cr[{\rm s}^{-1}]$$

which is exact for $N_{\rm H}$ =1.27 $\cdot$ 10^{20}cm^{-2} and the weighted mean spectral index $<\alpha_{\rm x}>$= 1.12 of the sources.

2.1.2. CFHT field

In order to fully utilize the sensitivity of the mosaic observation in the CFHT field the 9 PSPC photon event tables were merged and binned into a single image. By using events detected at off-axis angles $<30'$ the image covers a 2.9 deg^2 area with relatively homogeneous sensitivity $f_{\rm lim}$(1 keV) $\approx$ 2 nJy. As standard source detection algorithms failed due to the size of the image or tended to detect spurious sources at the FOV edges of the single pointings, we identified the X-ray sources by visual inspection of the smoothed image and found 149 pointlike sources. As the subset of X-ray sources investigated in this work have fluxes well above the detection limit, the source detection method is not thought to affect any of our results.

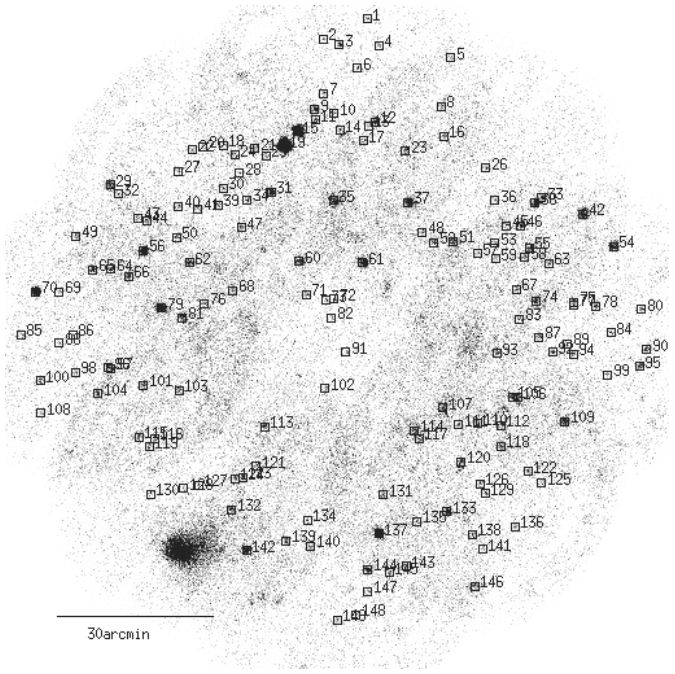

Fig. 2. ROSAT PSPC image of the CFHT field with source numbers as used in the text. The extended X-ray source in the lower left area is the cluster of galaxies Abell 1775.

Note that accidentally both the number of optically selected CFHT quasars and the number of X-ray sources is 149. The exact source positions were then determined by fitting two-dimensional Gaussian functions to the images of the sources. Fig. 2 shows the combined PSPC image with source numbers as used throughout this paper.

We extracted the source events in circular apertures with r=100" and the background in annuli of r=200-300" and produced count rate spectra by binning according to pulse height and subtraction of the background. We fitted power law models with galactic absorption fixed to $N_{\rm H} = 1.05 \cdot 10^{20}{\rm cm}^{-2}$ to the PSPC pulse height spectra and derived the spectral energy indices $\alpha_{\rm x}$ and flux densities at 1 keV for the 149 sources. When the number of detected counts did not permit a model fit with two free parameters, only the flux density at 1 keV was fitted with an assumed X-ray spectral index $\alpha_{\rm x} = 1.2$.

As 38 of the X-ray sources are associated with QSOs from the optical CFHT Quasar survey we were left with 111 ROSAT sources of unknown identification. Note that not all of the 65 X-ray detected CFHT quasars lie within the area covered by the central r =30' parts of the PSPC fields, which was used here for the selection of the X-ray sources.

2.2. Optical identification and spectral classification

2.2.1. SGP field

The spectroscopic observations in the SGP field have been performed with the ESO/MPIA 2.2m Telescope at La Silla during three nights (15-18 Nov. 1992). We used EFOSC2 (ESO Faint Object Spectrograph and Camera) to obtain long slit grism spectra of the optical candidates in the wavelength range $3500 - 9000$ Å. The 450 Å/mm grism yielded a resolution of 8.55 Å/pixel on the Thomson 1024×1024 CCD and a final resolution of 18 Å (FWHM).

As digitized versions of the southern sky surveys only recently became publicly available, we identified the optical counterparts in the SGP field using film copies of the ESO R and SERC J survey plates. For most of the 34 new ROSAT sources in the field only one candidate object is visible within the ROSAT PSPC error radius r=20". 6 X-ray sources do not have any counterparts brighter than the J plate limit at $m_{\rm B} \approx 21.5$ and two X-ray sources are clearly associated with bright stars. For two of the sources detected at large off-axis angles within the PSPC field of view the positional error is too large for the identification with optical objects. We were able to obtain spectra of optical counterparts for 23 X-ray sources (see Tab. 2). Meanwhile we have determined the optical positions and B magnitudes of the objects from a catalogue of objects based on digitized SERC J plates (Maddox et al. 1990).

2.2.2. CFHT field

For the CFHT field digitized POSS I survey data (APM survey, Irwin et al. 1994) had been available in advance of our spectroscopic observations and the identification of counterparts was based on source catalogues from blue POSS O and red POSS E plates. Spectroscopy in the CFHT field was carried out during five nights (17-22 Mar 1994) at the Calar Alto 3.5m Telescope equipped with the focal reducer, a 300 Å/mm grism, and a 1024×1024 pixel Tektronix CCD. Our grism spectra cover the wavelength range $3500 - 7800$ Å with 14 Å (FWHM) resolution. Priority was given to the 50 brightest X-ray sources corresponding to a flux density limit of 7 nJy at 1 keV. 16 of these sources do not have optical counterparts brighter than the POSS O limit $m_{\rm O}$ = 21.5, another 5 X-ray sources are associated with bright stars. For the remaining 29 bright X-ray sources spectra of 30 candidates in total were obtained (see Tab. 3). In addition spectra of 8 plausible quasar candidates with blue colour ($m_{\rm O} - m_{\rm E} < 1.5$) coinciding with X-ray sources fainter than 7 nJy were taken.

The spectra obtained both at La Silla and Calar Alto were extracted from the dark-subtracted and flat-fielded CCD frames using the ESO MIDAS long slit reduction routines. For relative flux calibration the standard stars LTT 2415 (ESO observations) and BD+28°2642 (Calar Alto observations) were used.

Finding charts for the objects both from the SGP and the CFHT fields can be retrieved along with the preprint of this paper via WWW at *http:\\astro.uni-tuebingen.de/publications/.*

2.3. Classifications and redshifts

For the identification of emission lines we have refered to the composite quasar spectrum from the Large Bright Quasar Survey as published by Francis et al. (1991).

Table 2. Identification statistics in the SGP field

#	f(1 keV) [nJy]	m_B	opt. spec.	z	M_{abs}	class.
1	125.29	14.5	+			star
2	25.11	20.0				
3	13.68	19.0	+	1.467	-26.9	QSO / Sy1
4	16.15	>21.5				EF[1]
5	4.95	>21.5				EF
6	10.76	>21.5				EF
7	25.83	20.0	+	1.085	-25.0	QSO / Sy1
8	9.77	21.0	+			
9	3.11	19.5				
10	14.20	19.5	+	1.486	-26.5	QSO / Sy1
11	34.00	15.0				star
12	11.05	21.0	+			star
13	20.37	20.0	+	1.028	-24.8	QSO / Sy1
14	24.11	19.5	+	0.413	-22.9	QSO / Sy1
15	2.93	>21.5				EF
16	4.10	20.0	+			star
17	6.14	>21.5				EF
18	221.32	17.5				PKS 0135-247
19	3.65	>21.5				EF
20	16.04	19.5	+	0.990	-25.2	QSO / Sy1
21	4.39	19.0	+	0.902	-25.5	QSO / Sy1
22	8.69	16.0	+			star
23	8.43	18.5	+			star
24	5.57	>21.5				EF
25	2.80	20.5	+			star
26	3.86	20.0	+	1.976	-26.9	QSO / Sy1
27	12.71	15.0	+			star
28	13.30	19.5	+	1.050	-25.4	QSO / Sy1
29	15.21	20.5				
30	36.97	18.5	+	0.218	-22.3	QSO / Sy1
31	59.51	18.0	+	0.306	-23.6	QSO / Sy1
32	189.88	18.0	+	0.358	-24.0	QSO / Sy1
33	10.83	18.5	+			star
34	171.60	18.0	+			star
35	91.51	>21.5				EF

[1] EF=empty field

In the SGP field we have identified 12 of the ROSAT sources with broad emission line AGN and measured their redshifts. 10 X-ray sources are associated with stars, in 12 cases the optical fields of the X-ray sources are empty or the identifications remain uncertain (see Table 2).

The 50 brightest X-ray sources in the CFHT field have been classified as follows: 15 broad emission line AGN, 7 narrow emission line galaxies (NELGs), one BL Lac object, 3 normal stars, and one normal galaxy. 17 X-ray positions are empty fields ($m_O > 21.5$) on the POSS O plates, another 6 identifications are unclear (see Table 3).

The redshifts of the emission line objects have been determined by averaging over individual redshifts of significantly detected emission lines for each object (see Tab. 4).

2.4. Remarks on individual sources

- *SGP 03 = RX J0137.9-241:* The optical spectrum of this quasar at z=1.476 shows absorption lines presumably caused by a galaxy 13" northeast of the quasar.
- *SGP 31 = RX J0138.7-2450:* The quasar (z=0.306) is identical with the quasar MS 0136.3-2505 (Stocke et al. 1991).
- *CFHT 15 = RX J1340.1+2743:* The object with the second highest X-ray flux in the CFHT field has a CCD magnitude of $\sim 22^m$ and its radio flux at 1.4 GHz is 3.9 mJy (Rengelink 1995, priv. comm.). The resulting broad band indices α_{rx} = 0.55 and α_{ox} = 0.71 are typical for an X-ray selected BL Lac object. The optical spectrum does not show any emission lines, from marginally detected absorption lines we derived the (uncertain) redshift z=0.205.
- *CFHT 21 = RX J1340.8+2740:* The spectrum of the quasar (z=1.900) shows absorption lines probably due to a galaxy 7" south of the quasar.
- *CFHT 114 = RX J1338.4+2644:* Two emission line objects were found in the positional error circle of the X-ray source. One object is a galaxy with strong [OII] emission at z=0.321, the other object is a quasar at z=0.595. As the optical spectrum of the galaxy differs from those of the other X-ray emitting galaxies, we assume the quasar to be the X-ray source.
- *CFHT 132 = RX J1341.1+2630:* The Seyfert 2 galaxy (z=0.070) is associated with the cluster of galaxies Abell 1775 (z=0.0695) and is located 11' northwest of the cluster center.

2.5. Luminosities and broad band spectral indices

Blue magnitudes m_B have been derived from the APM O plate data by applying the correction $m_B = m_O + 0.1$ (Evans 1988). We have calculated source frame continuum luminosities of the objects at 2500 Å and 2 keV using

$$\log(l_{opt}/[\mathrm{erg\,s^{-1}\,Hz^{-1}}]) = 38.257 - 0.4 m_B + 2\log(z(1+z/2)) + (\alpha_o - 1)\log(1+z) - \alpha_o \log(4400\ \text{Å}/2500\ \text{Å})$$

$$\log(l_x/[\mathrm{erg\,s^{-1}\,Hz^{-1}}]) = 34.63 + \log(f(1\ \mathrm{keV})/\mathrm{Jy}) + 2\log(z(1+z/2)) + (\alpha_x - 1)\log(1+z) - \alpha_x \log(2\ \mathrm{keV}/1\ \mathrm{keV})$$

(Zamorani et al. 1981). These formulae are valid for the cosmological parameters H_0 = 50 km s^{-1}Mpc^{-1} and q_0 = 0. The optical continuum is assumed to be a power law spectrum with the slope α_o = 0.5, the X-ray spectral index was set to α_x = 1.0. The optical luminosities have been corrected for interstellar extinction following Seaton et al. (1979) and the contribution of emission lines have been subtracted using the redshift dependent corrections given by Marshall et al. (1983).

The spectral energy distributions of the objects have been characterized by the broad band spectral indices α_{ox} calculated

Table 3. Identification statistics in the CFHT field

#	f(1 keV) [nJy]	m_B	opt. spec.	z	M_{abs}	class.
19	340.68	16.9	+	0.173	-23.4	NELG / Sy2
15	105.05	22.0	+			BL Lac
70	54.94	17.4	+	0.077	-21.0	NELG / Sy2
61	26.97	19.3	+	0.681	-24.4	QSO / Sy1
142	26.00	18.6	+	0.186	-21.9	NELG / Sy2
25	25.15	>21.5				EF[1]
33	24.67	20.1	+	0.809	-24.0	QSO / Sy1
106	20.41	>21.5				EF
144	19.88	20.4	+	0.986	-24.4	QSO / Sy1
120	19.67	13.3				star
9	17.84	19.7	+	0.656	-23.9	QSO / Sy1
107	17.03	10.8				star
11	16.99	21.2	+			
132	16.71	18.6	+	0.069	-19.6	NELG / Sy2
114	16.61	20.9	+	0.321	-21.2	QSO / Sy1
51	15.78	20.7	+	0.433	-21.8	NELG / Sy2
113	14.56	>21.5				EF
31	14.25	>21.5				EF
133	14.24	20.8	+	0.406	-21.6	QSO / Sy1
117	14.15	12.5	+	0.028	-23.7	galaxy
95	13.91	20.5	+	0.859	-23.9	QSO / Sy1
72	12.93	>21.5				EF
12	12.59	20.3	+	0.162	-19.8	NELG / Sy2
118	12.33	21.4				
124	12.30	>21.5	+			EF
129	12.09	21.2	+	0.604	-22.1	QSO / Sy1
3	11.99	21.0	+	0.740	-22.9	QSO / Sy1
78	11.74	20.3	+			
13	11.73	>21.5				EF
90	11.61	20.8	+	0.200	-19.8	QSO / Sy1
52	11.41	20.3	+	0.400	-22.0	QSO / Sy1
92	11.33	19.9	+	0.283	-21.6	NELG / Sy2
123	10.83	>21.5				EF
32	10.61	>21.5				EF
45	10.39	>21.5				EF
2	9.71	20.2	+	0.703	-23.5	QSO / Sy1
112	9.49	17.7				
23	9.00	>21.5				EF
35	8.83	20.9				
58	8.59	21.2	+	0.600	-22.1	QSO / Sy1
146	8.40	15.6				star
66	8.34	20.7	+	1.230	-24.7	QSO / Sy1
111	7.78	>21.5				EF
49	7.67	21.0	+	0.748	-22.9	QSO / Sy1
110	7.58	>21.5				EF
87	7.58	>21.5				EF
139	7.51	20.6				
89	7.45	>21.5				EF
30	7.44	>21.5				EF
14	7.31	>21.5				EF

[1] EF=empty field

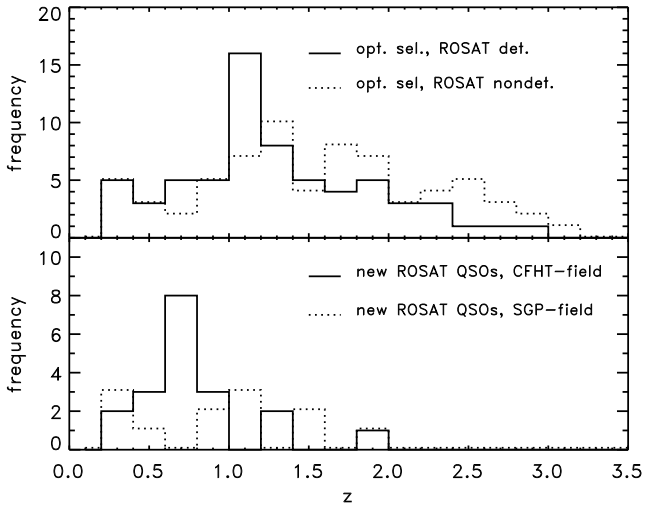

Fig. 3. Redshift distributions of X-ray selected and optically selected quasars.

from the source frame luminosity densities at 2500 Å and 2 keV:

$$\alpha_{ox} = \frac{\log l_{opt} - \log l_x}{\log \nu_{opt} - \log \nu_x} = \frac{\log l_{opt} - \log l_x}{2.606}$$

3. Results

3.1. Redshift distributions

The mean redshift in the optically selected sample ($\langle z \rangle$ = 1.46) is significantly higher than in the X-ray selected sample ($\langle z \rangle$ = 1.09). The lowest redshifts ($\langle z \rangle$ = 0.758) are measured in the subsample of 20 quasars identified from X-ray sources in the CFHT field, the majority of these objects is fainter than m_B = 20 as the optically brighter quasars were previously known from the optical survey. Because the sensitivity of the X-ray observations indicated by the number of detected QSOs per solid angle is comparable to the optical CFHT survey, the different redshift distributions cannot solely be attributed to different sensitivities in the X-ray and optical observations. The strong dependence of mean redshifts on the discovery waveband suggests a correlation of redshift and optical to X-ray energy distribution which is discussed in Sect. 3.3. Fig. 3 shows the redshift distributions of differently selected subsamples.

3.2. X-ray spectra

The broad band spectral indices α_{ox} and X-ray spectral indices α_x of the new ROSAT AGN are listed in Tab. 5. See Paper I for the corresponding data of the optically selected CFHT quasars. For both the optically selected quasars and the newly identified quasars we have calculated weighted mean values of the X-ray spectral indices α_x in bins of redshift z. The intervals z=[0-0.5], z=[0.5-1.0], z=[1.0-2.0], and z=[2.0-3.0] were used, however, the last bin contains none of the X-ray selected objects. The

Table 4. Positions and redshifts of ROSAT AGN

Source #	Catalog name	X-ray position α(2000)	X-ray position δ(2000)	opt. position α(2000)	opt. position δ(2000)	diff ["]	redshift	detected lines
			SGP field, QSO / Sy 1 (12 objects)					
3	RX J0137.9-2414	01 37 58.1	-24 14 29	01 37 59.01	-24 14 34.3	14	1.476	MgII,CIII],CIV
7	RX J0137.3-2419	01 37 21.6	-24 19 30	01 37 22.32	-24 19 49.2	22	1.085	MgII,CIII]
10	RX J0138.8-2423	01 38 48.9	-24 23 38	01 38 48.70	-24 23 32.9	6	1.486	MgII,CIII],CIV
13	RX J0138.1-2425	01 38 06.7	-24 25 12	01 38 06.66	-24 25 11.4	1	1.028	MgII
14	RX J0138.2-2425	01 38 13.2	-24 25 32	01 38 13.08	-24 25 35.7	4	0.413	[OIII],Hβ,MgII
20	RX J0137.3-2434	01 37 23.5	-24 34 58	01 37 23.62	-24 34 56.8	2	0.990	MgII
21	RX J0137.7-2435	01 37 47.1	-24 35 22	01 37 47.29	-24 35 24.3	4	0.902	CIII],CIV
26	RX J0137.5-2441	01 37 35.5	-24 41 20	01 37 35.62	-24 41 14.7	6	1.976	CIII],CIV,Lyα
28	RX J0137.1-2444	01 37 07.3	-24 44 48	01 37 07.68	-24 44 47.6	5	1.050	MgII,CIII]
30	RX J0137.4-2448	01 37 27.2	-24 48 34	01 37 27.44	-24 48 40.1	7	0.218	Hα,[OIII],Hβ,Hγ
31	RX J0138.7-2450	01 38 42.9	-24 50 35	01 38 43.33	-24 50 31.7	7	0.306	Hα,[OIII],Hβ,Hγ,MgII
32	RX J0139.9-2451	01 39 57.1	-24 50 43	01 39 57.73	-24 51 00.4	19	0.358	Hα,[OIII],Hβ,Hγ,MgII
			CFHT field, QSO/Sy 1 (19 objects)					
2	RX J1339.8+2801	13 39 48.0	+28 01 24	13 39 48.55	+28 01 45.2	23	0.703	[OII],MgII
3	RX J1339.5+2800	13 39 34.0	+28 00 18	13 39 34.16	+28 00 31.4	14	0.737	[OII],MgII
6	RX J1339.3+2755	13 39 17.9	+27 55 50	13 39 18.22	+27 55 60.0	12	0.710	MgII
9	RX J1339.9+2747	13 39 54.9	+27 47 48	13 39 55.56	+27 47 58.7	15	0.656	[OII],MgII
15	RX J1340.1+2743	13 40 10.4	+27 43 37	13 40 10.86	+27 43 47.8	13		
21	RX J1340.8+2740	13 40 47.6	+27 40 19	13 40 48.16	+27 40 09.5	13	1.900	CIII],CIV
33	RX J1336.6+2730	13 36 37.9	+27 30 45	13 36 37.68	+27 30 53.3	9	0.809	MgII
39	RX J1341.3+2729	13 41 18.9	+27 29 25	13 41 19.33	+27 29 27.3	8	0.480	MgII
49	RX J1343.3+2723	13 43 23.0	+27 23 12	13 43 23.71	+27 23 24.1	17	0.748	MgII
52	RX J1338.2+2722	13 38 11.4	+27 22 12	13 38 12.05	+27 22 06.3	13	0.397	MgII
61	RX J1339.2+2718	13 39 13.4	+27 18 20	13 39 13.25	+27 18 18.3	3	0.681	MgII
66	RX J1342.6+2715	13 42 37.1	+27 15 38	13 42 37.25	+27 15 41.3	4	1.229	MgII,CIII]
90	RX J1335.1+2701	13 35 08.3	+27 01 21	13 35 08.12	+27 01 39.5	19	0.200	[OIII],Hβ,[OII]
95	RX J1335.2+2658	13 35 14.5	+26 58 05	13 35 15.01	+26 58 14.2	13	0.860	MgII
114	RX J1338.4+2646	13 38 28.5	+26 45 50	13 38 29.53	+26 46 03.0	21	0.595	[OII],MgII
129	RX J1337.4+2633	13 37 28.5	+26 33 52	13 37 28.29	+26 33 52.8	3	0.605	MgII
133	RX J1338.0+2630	13 38 01.3	+26 30 14	13 38 01.50	+26 30 19.3	6	0.406	[OIII],Hβ,Hγ
144	RX J1339.1+2619	13 39 10.0	+26 19 07	13 39 09.80	+26 19 11.6	5	0.986	MgII,CIII]
147	RX J1339.1+2615	13 39 09.7	+26 14 51	13 39 09.37	+26 15 01.4	12	1.214	MgII,CIII]
			CFHT field, NELG (8 objects)					
12	RX J1339.0+2745	13 39 03.4	+27 45 29	13 39 03.70	+27 45 32.0	6	0.163	[OIII],[OII]
19	RX J1340.3+2740	13 40 22.5	+27 40 50	13 40 22.75	+27 40 58.3	9	0.173	[OIII],Hγ
51	RX J1337.9+2722	13 37 54.8	+27 22 24	13 37 55.10	+27 22 43.2	20	0.433	[OII]
70	RX J1343.9+2712	13 43 57.0	+27 12 27	13 43 57.36	+27 12 41.1	15	0.077	Hα,[OIII],[OII]
92	RX J1336.5+2701	13 36 29.7	+27 00 55	13 36 30.17	+27 01 01.1	10	0.283	[OIII],Hβ,[OII]
132	RX J1341.1+2630	13 41 07.3	+26 30 44	13 41 07.86	+26 30 48.9	11	0.070	Hα,[OIII],Hβ,[OII]
141	RX J1337.5+2623	13 37 30.8	+26 23 01	13 37 31.42	+26 23 11.9	15	0.646	Hγ,MgII
142	RX J1340.9+2622	13 40 54.4	+26 22 49	13 40 54.25	+26 22 53.7	5	0.183	[OIII],Hγ,[OIII]

resulting averages $\langle\alpha_x\rangle$ and the corresponding 1σ errors are listed in Tab. 6 and plotted in Fig. 4.

In both quasar samples the average spectra significantly flatten at higher redshifts, with the effect being even more pronounced in the X-ray selected sample. This redshift–α_x anti-correlation was previously found in ROSAT studies of optically and radio selected quasars (e.g. Schartel et al. 1992, Brunner et al. 1992) and can be interpreted as signature of the known X-ray spectrum of AGN with a hard power law component and a steep soft excess component extending to source frame energies $\lesssim 1$ keV. With increasing redshift the soft excess component is shifted out of the ROSAT PSPC sensitivity window and at higher redshifts the hard component dominates the measured

Table 5. Broad band and X-ray spectra

#	z	$\log l^1_{\rm opt}$	$\log l_{\rm x} \pm 1\sigma$	$\alpha_{\rm ox} \pm 1\sigma$	$\alpha_{\rm x} \pm 1\sigma$
			SGP field, QSO/Sy 1		
3	1.467	31.12	27.28±0.08	1.47±0.05	1.35±0.30
7	1.085	30.61	27.19±0.05	1.31±0.04	0.87±0.18
10	1.486	30.98	27.31±0.07	1.41±0.05	1.24±0.24
13	1.028	30.38	27.02±0.05	1.29±0.04	1.19±0.17
14	0.413	29.62	26.11±0.05	1.35±0.04	1.66±0.18
20	0.990	30.45	26.87±0.06	1.37±0.04	0.88±0.21
21	0.902	30.42	26.21±0.11	1.62±0.06	0.97±0.78
26	1.976	30.89	27.10±0.13	1.45±0.06	1.08±1.07
28	1.050	30.43	26.86±0.07	1.37±0.05	0.83±0.24
30	0.218	29.27	25.66±0.04	1.38±0.04	1.05±0.15
31	0.306	29.61	26.20±0.04	1.31±0.04	1.74±0.15
32	0.358	29.80	26.86±0.02	1.13±0.04	1.90±0.10
			CFHT field, QSO/Sy 1		
2	0.703	29.84	26.19±0.04	1.40±0.04	0.00±0.00
3	0.740	29.57	26.34±0.03	1.24±0.04	0.91±0.25
6	0.710	29.64	26.04±0.05	1.38±0.04	0.84±0.34
9	0.656	29.99	26.39±0.03	1.38±0.04	1.63±0.24
21	1.910	30.77	26.91±0.06	1.48±0.05	0.00±0.00
33	0.809	30.05	26.74±0.02	1.27±0.04	1.46±0.16
39	0.480	29.29	25.41±0.08	1.49±0.05	0.00±0.00
49	0.748	29.59	26.15±0.05	1.32±0.04	1.66±0.45
52	0.400	29.26	25.72±0.03	1.36±0.04	1.64±0.26
58	0.600	29.29	25.99±0.04	1.27±0.04	0.00±0.00
61	0.681	30.17	26.61±0.02	1.37±0.04	1.48±0.13
66	1.230	30.26	26.69±0.04	1.37±0.04	1.52±0.39
90	0.200	28.47	25.08±0.03	1.30±0.04	1.20±0.22
95	0.859	29.97	26.55±0.03	1.31±0.04	1.42±0.22
114	0.321	28.85	25.68±0.03	1.22±0.04	1.59±0.22
129	0.604	29.28	26.14±0.03	1.20±0.04	1.47±0.34
133	0.406	29.11	25.83±0.03	1.26±0.04	1.00±0.20
144	0.986	30.18	26.84±0.02	1.28±0.04	1.33±0.16
147	1.214	30.52	26.45±0.06	1.56±0.05	0.00±0.00
			CFHT field, NELG		
12	0.162	28.48	24.92±0.03	1.37±0.04	0.64±0.17
19	0.173	29.90	26.42±0.01	1.34±0.04	1.24±0.03
51	0.433	29.21	25.94±0.03	1.26±0.04	1.36±0.17
70	0.077	28.97	24.89±0.01	1.56±0.04	0.22±0.09
92	0.283	29.15	25.39±0.03	1.44±0.04	0.73±0.28
132	0.069	28.38	24.29±0.03	1.57±0.04	0.74±0.59
141	0.646	29.83	25.80±0.06	1.55±0.05	0.00±0.00
142	0.186	29.29	25.36±0.02	1.50±0.04	1.34±0.20

[1] Error of $\log l_{\rm opt}$ estimated to 0.1

spectrum. A quantitative discussion of the soft X-ray spectra in the context of an accretion disk model is given in Paper I.

For 7 of 8 narrow emission line objects we were able to fit single power law spectra to the X-ray spectra (from CFHT 141 = RX J1337.5+2623 too few counts were detected). When using models with fixed galactic absorption columns ($N_{\rm H}$ = $1.05 \cdot 10^{20}{\rm cm}^{-2}$), the resulting mean power law index $\langle\alpha_{\rm x}\rangle$ = 1.15 ± 0.03 is significantly harder than for the low redshift quasars either optically or X-ray selected.

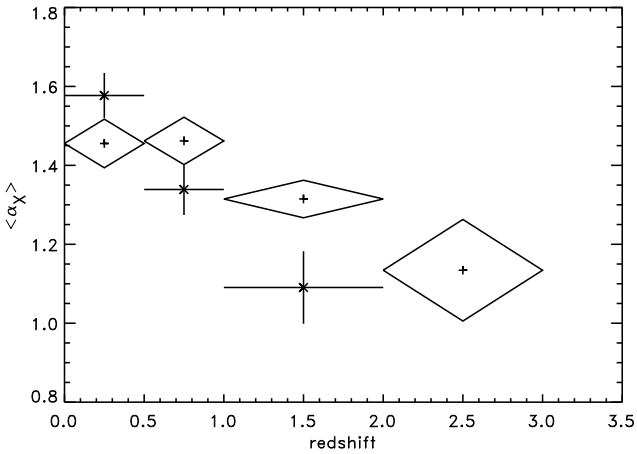

Fig. 4. Mean X-ray spectral indices $\alpha_{\rm x}$ of optically selected QSOs (plus signs with diamonds) and new ROSAT QSOs (crosses with error bars) in bins of redshift.

Table 6. Redshift averaged X-ray spectra

z	$\langle\alpha_{\rm x}\rangle \pm 1\sigma$	
	X-ray sel.	opt. sel
0.0–0.5	1.58 ± 0.06	1.46 ± 0.06
0.5–1.0	1.34 ± 0.06	1.46 ± 0.06
1.0–1.5	1.09 ± 0.09	1.31 ± 0.05
2.0–3.0	–	1.13 ± 0.13

As the signal to noise ratio of the X-ray spectra was generally too low for a determination of source frame absorption, we simulated the effect of intrinsic absorption in the NELGs on power law fits with galactic $N_{\rm H}$ to ROSAT PSPC spectra. Based on a source intrinsic power law spectrum with $\alpha_{\rm x}$ = 1.5, which is typical for the low redshift quasars, model spectra were calculated on a grid of redshifts and intrinsic absorption column densities. After additionally applying galactic absorption ($N_{\rm H}$ = $1.05 \cdot 10^{20}{\rm cm}^{-2}$) and folding the model spectra with the PSPC detector response, single power law spectra with absorption fixed to the galactic value were fitted to the simulated spectra. When the resulting spectral indices are compared with the fits to the narrow emission line AGN, the intrinsic absorbing column densities can be estimated (Fig. 5). Under the assumption of $\alpha_{\rm x}$ = 1.5 for the incident spectrum four objects are absorbed with intrinsic column densities $2.5 \cdot 10^{20}{\rm cm}^{-2} < N_{\rm H} < 5 \cdot 10^{20}{\rm cm}^{-2}$ and the spectra of three objects are consistent with no or little intrinsic absorption.

3.3. Luminosities and spectral energy distributions

We have investigated the dependence of the spectral energy distribution on luminosity and redshift for both the optically and X-ray selected quasar samples selected as follows:

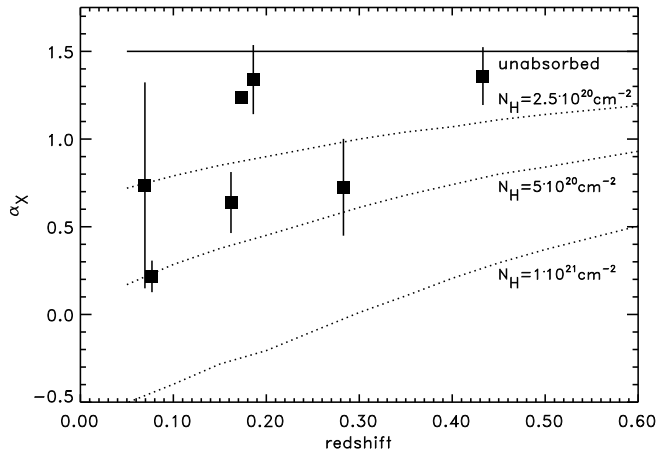

Fig. 5. Comparison of measured (full boxes) and simulated spectral fits of narrow emission line AGN with fixed galactic absorption of $N_{\rm H} = 1.05 \cdot 10^{20}{\rm cm}^{-2}$. The simulations assume intrinsic power law spectra with $\alpha_{\rm x} = 1.5$ without additional absorption (solid line) and intrinsic column densities $N_{\rm H} = 2.5{\cdot}10^{20}/5{\cdot}10^{20}/1{\cdot}10^{21}{\rm cm}^{-2}$ (dotted lines).

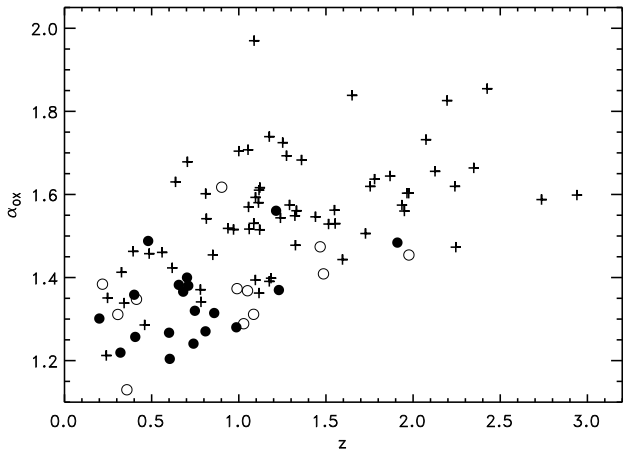

Fig. 6. Optical to X-ray spectral indices $\alpha_{\rm ox}$ vs. redshift for optically selected QSOs (plus signs), ROSAT QSOs in the CFHT field (full dots) and in the SGP field (open circles).

1. *Optically selected sample:* The sample comprises 134 CFHT survey quasars. 65 of these quasars are X-ray detected, 69 have X-ray upper limits, the remaining 15 of the originally 149 CFHT quasars were not included due to source confusion or large deviations between X-ray and optical positions (see Paper I for details on this sample).
2. *X-ray selected sample:* The sample as used in this section was compiled from the X-ray selected quasars in the SGP field (12 objects) and from the newly identified quasars in the CFHT field (19 objects). Those quasars from the optical CFHT survey were included in the X-ray selected sample, which coincided with one of the 149 X-ray sources (see Fig. 2) and have X-ray fluxes $>$ 10 nJy (16 objects, see Table 7). By using this selection a completeness level of 75% (38/51) in the identification of the CFHT field X-ray sources above 10 nJy was achieved.

In the optically selected sample a clear correlation of $\alpha_{\rm ox}$ and redshift exists (Fig. 6); a Spearman-Rank test yields a chance probability $< 10^{-5}$. The new ROSAT QSOs on average have lower $\alpha_{\rm ox}$ values and, as shown in Sect. 3.1, were found at lower redshifts than the optically selected quasars. The X-ray selected objects thus populate the lower left area in the $\alpha_{\rm ox}$ (z) diagram, as is predictable from the correlation observed in the optically selected sample.

Due to the tight correlations of luminosities and redshifts in flux limited samples correlations of any parameters with redshift also induce correlations with luminosity and vice versa. In principle the underlying relation can be found by applying a two-dimensional regression analysis with redshift and luminosity as independent variables. An implementation of this method which also handles upper or lower limits of the dependent variable is the DB (detections and bounds) regression analysis (Avni&Tananbaum 1986). We used it under the assumption

Table 7. Broad band spectra of CFHT survey quasars included in X-ray selected sample.

#[1]	z	[2] $\log l_{\rm opt}$	$\log l_{\rm x} \pm 1\sigma$	$\alpha_{\rm ox} \pm 1\sigma$
19	0.783	30.48	26.99±0.02	1.34±0.04
26	1.116	30.71	27.16±0.03	1.36±0.04
29	0.560	29.58	25.77±0.09	1.46±0.05
35	1.440	30.98	26.96±0.06	1.55±0.04
36	0.780	30.28	26.71±0.04	1.37±0.04
43	1.549	31.05	26.98±0.05	1.56±0.04
69	0.342	29.47	25.98±0.02	1.34±0.04
80	0.240	29.10	25.94±0.02	1.21±0.04
83	1.113	30.83	26.71±0.08	1.58±0.05
111	1.095	30.30	26.67±0.05	1.39±0.04
113	1.175	30.49	26.86±0.04	1.39±0.04
119	1.185	30.94	27.29±0.02	1.40±0.04
124	0.705	31.10	26.72±0.02	1.68±0.04
130	0.810	30.86	26.68±0.04	1.60±0.04
131	2.737	31.63	27.49±0.06	1.59±0.05
142	2.245	31.19	27.35±0.06	1.47±0.05

[1] Object numbers from Crampton et al. 1989 .
[2] Error in $\log l_{\rm opt}$ estimated to 0.1 .

of Gaussian residuals with standard deviation σ of the measured data points from the fit function. The method minimizes the function

$$S = -2 \ln L = \sum_i \left(\frac{r_i^{\rm D}}{\sigma} \right)^2 + 2N_{\rm D} \ln \sigma - 2 \sum_j \ln F_{\rm G} \left(\frac{r_j^{\rm B}}{\sigma} \right) + N_{\rm D} \ln(2\pi)$$

to find the best fit regression at the maximum of the likelihood function L and estimates confidence intervals assuming χ^2 distribution of S .

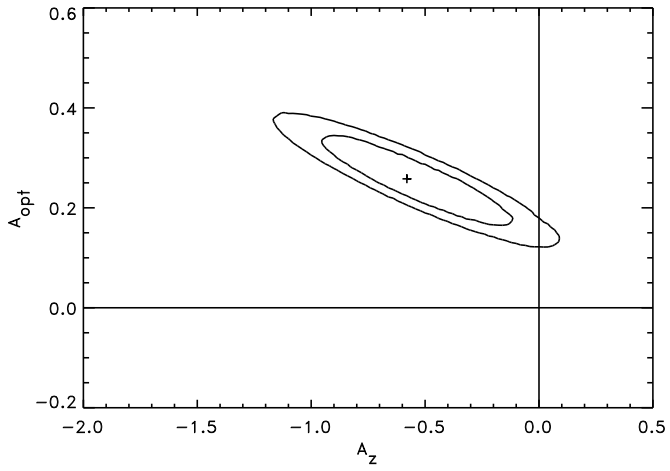

Fig. 7. 68% and 90% confidence contours for the parameters A_z and A_{opt} derived from fitting the dependence of α_{ox} on redshift and optical luminosity in the optically selected quasar sample.

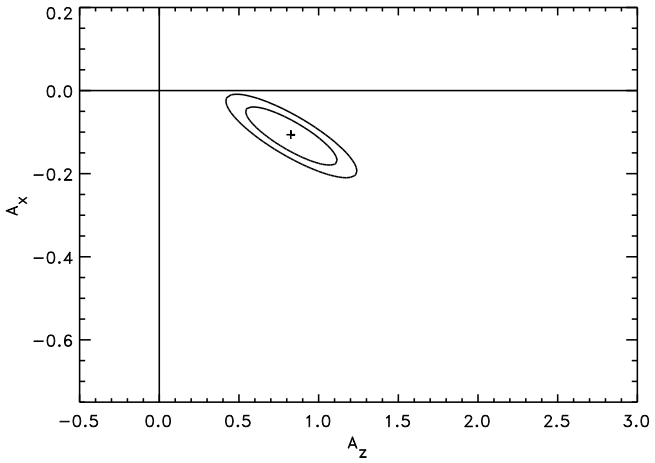

Fig. 8. 68% and 90% confidence contours for the parameters A_z and A_x derived from fitting the dependence of α_{ox} on redshift and optical luminosity in the X-ray selected sample.

$F_G(x)$ is the cumulative standard Gaussian probability

$$\int_x^\infty dy \frac{1}{\sqrt{2\pi}} e^{-(1/2)y^2}$$

and r_i^D are the residuals of N_D detections and r_j^B the residuals of N_B bounds. We have used the DB method to calculate confidence contours of the linear coefficients A_{opt} and A_z describing the dependence of the mean α_{ox} on optical luminosity and lookback time $\tau(z) = z/(z+1)$ for the optically selected sample (65 X-ray detections, 69 X-ray upper limits). Following Avni&Tananbaum we have used the fit function have been derived correspondingly.

$$\langle \alpha_{ox} \rangle = A + A_z(\tau(z) - 0.5) + A_{opt}(\log l_{opt} - 30.5) \quad (1)$$

For the X-ray selected sample (47 objects) the parameters A_x and A_z of the function

$$\langle \alpha_{ox} \rangle = A + A_z(\tau(z) - 0.5) + A_x(\log l_x - 30.5) \quad (2)$$

In the optically selected sample the regression coefficients are $A_z = -0.58 \pm 0.75$ and $A_{opt} = 0.26 \pm 0.13$ (Fig. 7). The errors were determined from 90% confidence contours (ΔS = 4.6 for 2 interesting parameters). The best fit values for the intercept and the width of the residuals are $A = 1.67$ and $\sigma = 0.183$.

In the X-ray selected sample the regression analysis yielded $A_z = 0.83 \pm 0.35$, $A_x = -0.11 \pm 0.09$, $A = 1.44$, and $\sigma = 0.10$ (Fig. 8). The results from the optically selected sample suggest that α_{ox} primarily depends on optical luminosity, while the z-dependence is not significant or even negative. On the other hand, the analysis of the X-ray selected sample yield a significant dependence of α_{ox} on $\tau(z)$. This apparent discrepancy is weakened by the results of simulations of the sample properties as discussed in Sect. 3.4.

Assuming that no explicit dependence of α_{ox} on z exists, the problem is reduced to the relation of l_x on l_{opt}. A variation of $\langle \alpha_{ox} \rangle$ with l_{opt} implies a nonlinear relation of l_x and l_{opt}. We therefore have investigated this relation using the DB method and find

$$\log l_x = (26.14 \pm 0.12) + (0.62 \pm 0.18)(\log l_{opt} - 30.5)$$

for the optically selected sample. Note that the consideration of X-ray upper limits largely eliminates the influence of selection effects. For the X-ray selected sample

$$\log l_{opt} = (30.11 \pm 0.09) + (1.16 \pm 0.17)(\log l_x - 26.5)$$

was obtained (errors correspond to 90% confidence). Calculating the reverse regression $\log l_x(\log l_{opt})$ in the X-ray selected sample, which is strictly speaking incorrect because of biasing due to X-ray flux limits, we obtain

$$\log l_x = (26.78 \pm 0.09) + (0.71 \pm 0.11)(\log l_{opt} - 30.5)$$

yielding a similar slope as in the optically selected sample. The nonlinearity in the l_x - l_{opt} relation (evident as deviation of the slope from unity in the relation of the logarithmic luminosities) is very significant in the optically selected sample and significant at the $\sim$ 90% level in the X-ray selected sample. The result implies that optically luminous objects are subluminous in X-rays.

3.4. Simulation of sample characteristics

In order to interpret the results of the DB regression analysis of $\alpha_{ox}(l, z)$ we have simulated quasar samples of the same size as the CFHT optical sample using two different methods.

In one case we took the redshifts and optical luminosities of the CFHT quasars as input and calculated simulated broad band spectral indices α_{ox} according to the fit function (Eq. 1)

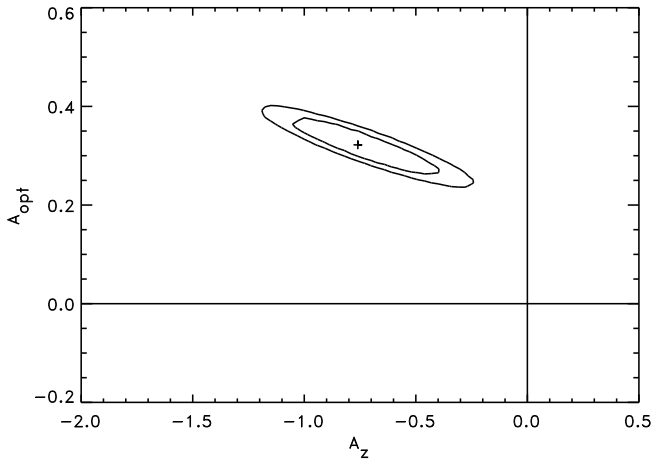

Fig. 9. 68% and 90% confidence contours of the parameters A_z and A_{opt} for the simulated sample.

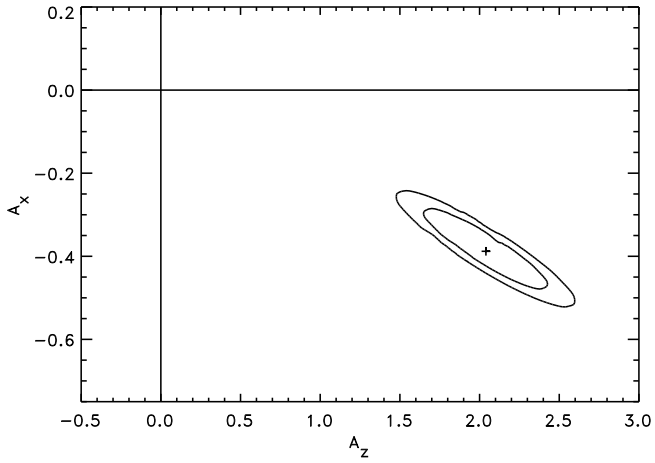

Fig. 10. 68% and 90% confidence contours of the parameters A_z and A_x for the simulated sample.

used in the regression algorithms plus random deviates with Gaussian distribution. When the 1 keV flux density resulting from l_x and redshift dropped below 4 nJy at 1 keV, the luminosity corresponding to this flux value was taken as upper limit and the object treated as not detected in X-rays. A lower limit of α_{ox} value was then calculated from the optical luminosity and the X-ray luminosity corresponding to $f_x(1\ keV)$ = 4 nJy. For all realizations of the simulation the DB method was able to reliably recover the input parameters A_z, A_{opt}, A, and σ within the statistical errors.

In the second case, using the redshifts of the CFHT quasars as input, the mean optical and X-ray luminosities have been calculated using the relations

$$\langle \log l_{opt} \rangle = 2.6 \cdot \log z + 30.6$$

and

$$\langle \log l_x \rangle = 1.7 \cdot \log z + 26.5\ .$$

The slopes and intercepts of these relations had been derived from DB regressions on the real quasar sample. The luminosities of the individual objects in the simulated sample were then calculated by addition of random deviates with Gaussian distribution of the width σ = 0.3. X-ray "detections" and "upper limits" were simulated in the same way as in the above case. For the particular realization discussed here this process resulted in 68 "detections" and 66 "non-detections". The full sample (detections and non-detections) was taken as optically selected model sample and the 68 X-ray detections were taken as X-ray selected model sample. Using the DB method with Eq. 1 in the same way as for the quasar data we derived the slopes $A_z = -0.76 \pm 0.48$ and $A_{opt} = 0.32 \pm 0.08$ in the simulated sample (optically selected). The slopes $A_z = 2.04 \pm 0.57$ and $A_x = -0.39 \pm 0.15$ (Eq. 2) resulted from the analysis of the X-ray selected model sample. Figs. 9 + 10 show the corresponding confidence contours and can directly be compared with Figs. 7 and 8.

These results are in qualitative agreement with the analysis of the optically and X-ray selected quasar samples. In particular the simulation shows that the regression can lead to completely different values of A_z, depending whether it is fitted with A_{opt} in the optically selected sample or A_x in the X-ray selected sample, although the simulation used the same input regression parameters for both samples. The reason for these inconsistencies is the fact that α_{ox} is not statistically independent from the luminosities. As it is calculated as $\alpha_{ox} = (\log l_{opt} - \log l_x)/2.606$, the resulting coefficients from the analysis of a sample with completely random luminosities would be $A_{opt} = 1/2.606 = 0.384$ and $A_x = -0.384$. This effect, together with the tight correlation of luminosities and redshifts in any flux limited samples, hampers attempts to disentangle the effects of luminosity and redshift on the broad band spectrum regardless of the regression method used.

4. Discussion

Our identifications of ROSAT sources in two fields of low galactic absorption have resulted in a sample of 39 new X-ray selected quasars and 8 narrow emission line galaxies. The fact that most of the new ROSAT quasars in the optical CFHT quasar survey field are fainter than $m \sim 20.0$ confirms the completeness of the optical survey above this flux level.

4.1. X-ray spectra

The investigation of the X-ray spectra in the optically selected and X-ray selected quasar samples lead to largely consistent results in both samples. The mean X-ray power law indices drop from $\langle \alpha_x \rangle \sim 1.5$ at z=0-0.5 to $\langle \alpha_x \rangle \sim 1.1$ in the highest redshifts bin (z=1.0-2.0 for the X-ray selected objects, z=2.0-3.0 for the optically selected sample). We interpret this correlation as evidence for a soft excess which is shifted out of the PSPC sensitivity window for higher redshifts (see also Paper I).

For the ROSAT selected AGN sample from the RIXOS survey Puchnarewicz et al. (1996) report $\langle \alpha_x \rangle$ = 1.07 being inde-

pendent of redshift. This discrepancy is probably attributed to the fact that the RIXOS survey due to the selection of X-ray sources in the harder 0.4-2.0 keV energy band is more sensitive to intrinsically absorbed sources. The spectral fits with fixed galactic $N_{\rm H}$ applied to the RIXOS AGN yield low spectral indices for absorbed sources at low redshifts and the absorbed objects may thus compensate the contributions of soft excess sources to the mean spectral index.

We only find evidence for intrinsic absorption in the X-ray spectra of some of the narrow emission line objects, the source intrinsic column densities are estimated to be $N_{\rm H} \leq 5 \cdot 10^{20}{\rm cm}^{-2}$.

4.2. Spectral energy distributions

The dependence of $\alpha_{\rm ox}$ on optical luminosity and redshift have been investigated by Avni&Tananbaum (1986) and Wilkes et al. 1994 in optically selected quasar samples observed by the *Einstein* satellite. The latter authors give $A_{\rm opt} = 0.10 \pm 0.04$ and $A_{\rm z} = 0.006 \pm 0.17$ (1σ errors) for a large heterogeneous sample compared to $A_{\rm opt} = 0.26 \pm 0.09$ and $A_{\rm z} = -0.58 \pm 0.48$ in our optically selected sample. Our ROSAT results are derived from fainter sources with higher average redshift but are qualitatively consistent with the *Einstein* measurements. Apparently the primary correlation is $\alpha_{\rm ox}(\log l_{\rm opt})$ which is somewhat steeper in our data.

Green et al. 1995 used the ROSAT All Sky Survey (RASS) data of the Large Bright Quasar Survey (LBQS, Hewett et al. 1991) to investigate the spectral energy distributions in a homogeneous sample. As only $\sim 10\%$ of the quasars were detected in the RASS, the authors used a stacking method to incorporate the data of the undetected objects. They measured the relation

$$\alpha_{\rm ox} = (1.44 \pm 0.7) + (0.08 \pm 0.02)(\log l_{\rm opt} - 30.5)$$

in this sample of relatively bright quasars ($m < 19.0$) assuming no explicit redshift dependence.

The ROSAT observations of the CFHT survey field for the first time enable us to investigate the dependencies of $\alpha_{\rm ox}$ with z and luminosity in a complete optically selected quasar sample based on homogeneous X-ray data with a high detection rate.

The first investigation of this kind in an X-ray selected sample was published by Pickering et al. (1994) who applied the DB regression method to the relation $\alpha_{\rm ox}(\tau(z), \log l_{\rm x})$ in the EMSS (Gioia et al. 1990) quasar sample and report a significant redshift dependence of $\alpha_{\rm ox}$ with $A_{\rm z} = 0.79$ and an anti-correlation with $\log l_{\rm x}$ ($A_{\rm x} = -0.17$) similar to the relations in our X-ray selected sample. As the EMSS sample in this regard seemed to differ significantly from optically selected samples, they infer that different populations of quasars may be selected in optical and X-ray surveys. From the simulations presented in Sect. 3.4 we conclude that the strong $\alpha_{\rm ox}$ -redshift correlation and the $\alpha_{\rm ox}$ -$\log l_{\rm x}$ anti-correlation in the X-ray selected samples are spurious and that the intrinsic relations are consistent with those in the optically selected sample. However, due to the obviously limited possibility of disentangling the effects of redshift and luminosity we cannot exclude an explicit relation of $\alpha_{\rm ox}$ and redshift in either of the samples.

We do not find a correlation of $\alpha_{\rm ox}$ and X-ray spectral index $\alpha_{\rm x}$ as Puchnarewicz et al. (1996) report for the RIXOS AGN. The correlation in the RIXOS sample is largely caused by a group of presumably absorbed sources with particularly low $\alpha_{\rm ox}$ and $\alpha_{\rm x}$. Therefore the difference with respect to the RIXOS result is probably due to the above stated absence of a large number of absorbed objects in our sample.

5. Conclusions

We have used deep ROSAT observations of an optical quasar survey field and a sample of 31 new soft X-ray selected quasars to compare the X-ray properties of optically and X-ray selected quasars. We do not find significant differences in the mean X-ray spectra of the two samples, in both samples the soft excess component is evident from the anti-correlation of $\alpha_{\rm x}$ and redshift. There is no evidence for a large number of intrinsically absorbed sources in the X-ray selected sample of broad emission line AGN neither from the X-ray spectra nor from the optical to X-ray energy distributions. In both samples we find that optically luminous objects are underluminous in X-rays, but also cosmological evolution of the spectral energy distribution towards X-ray brighter objects at low redshifts cannot be ruled out.

From the consistent properties of both samples we conclude that the X-ray and optically selected quasars belong to the same population of objects with X-ray selection favouring objects with lower $\alpha_{\rm ox}$ and lower redshifts.

Acknowledgements. We would like to thank Mike Irwin and Gavin Dalton for providing the APM digitized survey data for the two ROSAT fields. We thank the staffs of the European Southern Observatory and the Calar Alto Observatory for their assistance during the observation runs. This work was supported by DARA under grants 50 OR 9009, 50 OR 9603, and 50 QR 8802.

References

Arnaud, K.A., Branduardi-Raymont, G., Culhane, J.L, et al. 1985, MNRAS, 217, 105
Avni, Y., and Tananbaum, H. 1986, ApJ 305, 83
Boyle, B.J., Griffith, R.E., Shanks, T., Steward, G.C., and Georgantopoulos, I. 1993, MNRAS, 260, 49
Boyle, B.J., McMahon, R.G., Wilkes, B.J., and Elvis, M. 1995, MNRAS, 272, 462
Brunner, H., Friedrich, P., Zimmermann, H.-U., and Staubert, R. 1992, in "X-ray emission of AGN and the cosmic X-ray background", eds. W. Brinkmann and J, Trümper, Garching 1992, p. 198
Brunner, H., Lamer, G., Dörrer, Th., Friedrich, P., and Staubert, R. 1996, A&A, in preparation, (Paper I)
Comastri, A., Setti, G., Zamorani, G., and Hasinger, G., et al. 1995, A&A, 296, 1
Crampton, D., Cowley, A. P., and Hartwick, F. D. A. 1989, ApJ, 345, 59
Evans, D. 1988, PhD thesis, University of Cambridge
Francis, P.J., Hewett, P.C., Foltz, C.B., et al. 1991, ApJ, 373, 465
Green, P.J., Schartel, N., Anderson, S.F., et al. 1995, ApJ, 450, 51

Gioia, I.M., Maccacaro, T., Schild, R.E., et al. 1990, ApJS, 72, 567
Hasinger, G., Burg, R., Giaconni, R., et al. 1993, A&A, 275, 1
Hewett, P.C., Foltz, C.B., Chaffee, F.H. et al. 1991, AJ, 101, 1121
Irwin, M.J., Maddox, S.J., and McMahon, R.G. 1994, Spectrum, 2, 14
Maddox, S.J., Efstathiou, G., Sutherland, W.J., and Loveday, J. 1990, MNRAS 243, 692
Marshall, H. L., Tananbaum H., Zamorani, G., et al. 1983, ApJ, 269, 42
Pickering, T.E., Impey, C.D., and Foltz, C.B. 1994, AJ, 108, 1542
Puchnarewicz, E.M., Mason, K.O., Romero-Colmenero, E., et al. 1996, MNRAS, 281, 1243
Rengelink, R. 1995, private communication
Schartel, N., Walter, R, Fink, H.H. 1992, in "Multi-wavelenght continuum emission of AGN", eds. Courvoisier, T.J.-L. and Blecha, A., IAU Symp. 159, 373
Seaton, M. J. 1979, MNRAS, 187, 75
Stark, A.A., Gammie, C.F., Wilson, R.W., et al. 1992, ApJS, 79, 77
Stocke, J.T., Morris, S.L., Gioia, I.M., et al. 1991, ApJS, 76, 813
Wilkes, B.J., Tananbaum, H., Worrall, D.M., et al. 1994, ApJS, 92, 53
Zamorani, G., Henry, J. P., Maccacaro, T., et al. 1981, ApJ, 245, 357

This article was processed by the author using Springer-Verlag LaTeX A&A style file *L-AA* version 3.